An image processing approach for polishing metal additive manufactured components to improve the dimensional accuracy and surface integrity

Abhilash Puthanveettil Madathil [1]*, Afzaal Ahmed [2]

[1] Centre for Precision Manufacturing, DMEM, University of Strathclyde, Glasgow, G1 1XJ, UK

[2] Department of Mechanical Engineering, Indian Institute of Technology Palakkad, Kerala, 678557, India

Corresponding author: abhilash.p-m@strath.ac.uk; ORCID ID: 0000-0001-5655-6196

Abstract: Metal additive manufacturing (MAM) process has gained enormous popularity in past few decades due to its capability to fabricate the components in near-net-shape with minimal material wastage. Owing to its flexibility to produce complex/ intricate shapes, the process has found several applications in the aerospace, automobile and biomedical industries. However, wide industrial acceptance of the MAM components is lagging because of their poor dimensional accuracy and surface integrity which limits the functionality and achievable tolerances when compared to the subtractive manufacturing methods. Thus, a post-processing strategy is needed to enhance the dimensional accuracy and surface integrity of the additive manufactured components. Manual inspection of various features, especially corner profiles can be expensive, time-consuming and inaccurate. Ti6Al4V alloy has wide applications in aerospace, biomedical and marine industries due to its superior properties like strength-to-weight ratio, biocompatibility and fatigue resistance. This article presents an image processing approach for improving the corner accuracy and surface integrity of selective laser melted (SLM) Ti6Al4V components using wire electric discharge polishing (WEDP). Subsequently, fourteen components with different corner profiles, namely acute ($\theta = 30^{O}$), orthogonal ($\theta = 90^{O}$), and obtuse ($\theta = 120^{O}$), were fabricated by varying laser power, hatch distance and scan speed. Minimum polishing depth has been evaluated by capturing the raw images of MAM components and the corner profiles are extracted using an image processing approach. A significant improvement in dimensional accuracy of 80.7 %, 77.3 % and 85.4 % were obtained for orthogonal, acute and obtuse profiles respectively after WEDP. Moreover, the surface roughness (S_z) reduction from ~ 61.86 μm to ~8.41 μm was achieved along with removing micro pits and voids, waviness and balling defects from the surface. EDS analysis showed that only a negligible amount of Zn (0.57 wt. %) and Cu (0.8 wt. %) is present over the finished surface. Based on the above findings, WEDP showed excellent capabilities in conjunction with an image processing approach to enhance the dimensional accuracy and surface integrity of metal additive manufactured components.

Keywords: Metal additive manufacturing, WEDP, Ti_6Al_4V, Image Processing, Corner accuracy, Surface Integrity

1. Introduction

The metal additive manufacturing (MAM) process is extensively used in industries globally due to its advantages over subtractive manufacturing processes like lower material wastage, reduced costs, and near-net-shape production. However, the metal additive manufactured component's accuracy, repeatability, and surface finish need substantial improvements to widen its industrial application. Among various metal AM processes, selective laser melting (SLM) is relatively inexpensive, handles a wider range of materials and gives desirable mechanical properties. SLM involves layer-by-layer melting of metal powders by a laser under an inert atmosphere. However, MAMed components are not suitable for direct use, due to their poor surface finish, dimensional inaccuracy, poor wear and corrosion characteristics and high tensile residual strength. The inferior surface integrity is caused due to the effects like balling, stair-stepping, partially melt powders, lack of fusion, etc. Also, since this is a thermal process, inherent residual stresses can cause micro-cracks and other micro defects in the surface. Such micro defects can act as crack nucleation sites restricting the component's mechanical strength, especially in high-temperature applications. Due to the layer-by-layer manufacturing phenomena, the achievement of sharp corners is another reported challenge.

The surface integrity of MAMed components can be improved to some extent by optimizing the process parameters like scan speed, laser power, hatch spacing, layer thickness, and scan strategy. However, additional post-process treatments are desirable for most industrial applications. MAMed components are conventionally post-processed by mechanical, thermal, chemical, or hybrid means, but most of these techniques have severe limitations. Also, since the post-processing operations will result in reduced part, knowledge of minimum polishing depth is of great relevance to minimize material wastage and control dimensional accuracy. Manual inspection and computation of polishing depth will be time-consuming and inefficient. Manual inspections of components are being replaced by image processing systems in manufacturing industries to detect part defects and extract relevant information. The paper presents an image processing approach to compute the minimal polishing depth to enhance corner accuracies of MAMed components. WEDP, an electrical discharge-based hybrid polishing technique is used in this study due to its several advantages over the existing conventional techniques for post-processing.

2. Literature Review

Several researchers have investigated various methods to enhance the geometric accuracy and surface integrity of MAMed components in recent years. A detailed literature review of such studies is given in this section.

2.1 Studies on corner accuracies

The accuracies of various benchmark features built by MAM have been explored by several researchers in the past [1, 2]. In those studies, MAMed components are reported to have several limitations in producing sharp corners, i.e., near zero-radius at the surface interjection. Unlike the CAD file fed to the system, the printed components will always have a rounded corner. Limited literature is available that investigates the challenges of the MAM process to achieve good corner accuracy. Kruth et al. [3] compared the capability of 5 different metal 3D printers to produce several benchmark features. Several dimensional and geometric accuracies are studied, namely corner accuracy, length, width, height, hole diameter, cylinder diameter, thin wall thickness, stair effect, curl effect, and overhangs. It was found through this experimental study that the EOS machine was particularly good at achieving sharp corners. The authors observed that the layer thickness, scanning errors, and heat accumulation restricts the building of sharp part corners. The capability of the MAM-built Ti6Al4V and CoCrMo in manufacturing medical implants was investigated by Vandenbroucke and Kruth [4]. 2 benchmark designs are printed which contain several sharp edges ranging from angles 15^{O} to 45^{O} to study the part's accuracy. The overall dimensional accuracy reported in the study was less than 40 μm. However, specific details about the corner accuracy studies were not presented.

A scanning strategy to achieve better corner sharpness during the MAM process was proposed by Luo et al. [5]. It was found that the corner inaccuracies are associated with the non-uniform scan speeds at the corners. A skywriting loop strategy was devised to eliminate this effect and to maintain a uniform scanning velocity at the corners. Schwanekamp et al. [6] reported that the corner and edge sharpness is dependent on the melt pool geometry by investigating MAM fabricated carbide cutting tools with complex geometries. In another study, Han et al. [7] studied the angle of corners considering 8 different orthogonal corners. It was experimentally found that corner angle accuracy was dependent on the scanning strategy and a square-framed scanning method maximizes the corner angle accuracy. Braian et al. [8] explored the feasibility of using MAM built components in dentistry by comparing their precision and accuracy with subtractive manufactured components. The additive manufactured components are reported to deviate significantly from the CAD file, especially with respect to corner accuracy. Subtractive manufacturing was considerably better with respect to corner accuracy for multiple test specimens. The inability of the MAM process to produce the components with sharp corner radii is reported to be due to the stair effect and surface roughness. Matache et al. [9] reported elevated ridge defects on corners due to melting pool behaviour during the cooling cycle. The microstructural analysis also revealed that the corner edges were significantly rounded, contrast to the CAD file. The corner ridges are found to increase with laser power and decrease with scanning speed.

2.2 Polishing methods

Earlier research have proven that post processing is inevitable for MAMed components to counter the effects of poorer surface finish and geometric inaccuracies. There are various finishing methods for metal additive manufactured components such as laser polishing, chemical polishing, abrasive finishing, and mechanical polishing. Zhihao et al. [10] conducted laser polishing on MAM-Inconel 718 and reported an improvement in surface roughness (R_a) from ~ 7 μm to ~ 0.1 μm. A layer polishing strategy by automatic adjustment of focussing distance was proposed by Yung et al. [11]. Using this approach, a reduction in surface roughness (S_a) of 93% was reported in this study. A femtosecond laser polishing is reported to improve the surface roughness (R_a) from 4 μm to 0.8 μm during the post processing of Ti6Al4V MAM fabricated components by Worts et al. [12]. Scherillo [13] introduced a multi-step chemical polishing strategy where the chemical machining is preceded by a brightening operation. An electrochemical polishing approach to finish the MAM fabricated Inconel 718 components was proposed by Jain et al. [14]. At optimal parameter settings, the proposed polishing operation was able to reduce the surface roughness (R_a) to 0.25 μm. An abrasive flow machining method was reported to be successful in removing the balling and lack of fusion defects from the additive manufactured surfaces [15]. Also, a reduction of surface roughness (S_a) from 13 μm to 1.8 μm was reported in this study. Tan and Yeo [16] found an enhancement in the microhardness of additive manufactured Inconel 625 components after ultrasonic cavitation abrasive finishing. Zhang et al. [17] have implemented a magnetic abrasive finishing of MAM 316L steel and reported a substantial surface roughness (R_a) reduction of 75 %. In addition, an analytical equation was developed correlating Ra, and productivity. Bagehorn et al. [18] performed a comparison of milling, micromachining, blasting, and vibratory grinding and reported the performance of milling to be superior to the other polishing methods. Mechanical polishing methods to improve the surface integrity of MAM fabricated Inconel 718 were explored by Kaynak and Tascioglu [19]. A considerable improvement in surface roughness (R_a, from 19 μm to 1.8 μm) and microhardness (from ~320 HV to ~375 HV) was reported after polishing.

All the aforementioned processes are associated with several limitations. For example, the processing time for laser polishing is high due to the small laser spot size. Chemical polishing is difficult to control and is considered unsustainable due to the difficulty in handling and disposal of chemicals. Abrasive finishing results in the impingement of micro-abrasive particles onto the finished surface. Also, the process is not recommended to finish intricate and internal profiles. Mechanical polishing is relatively expensive, cannot finish complicated profiles and often unfavourably alters the mechanical properties of the component. In this context, hybrid finishing methods have been proposed by a few researchers in the past to overcome the limitations of these conventional finishing methods. WEDP is one such process that has been reported to considerably improve the surface integrity of SLM components [20, 21].

2.3 Image processing based defect detection systems

Several researchers have developed image processing based online inspection systems for additive manufacturing processes. Zhang et al. [22] have proposed a convolutional neural network (CNN) that accurately classifies the MAM parts into defective and non-defective categories based on the quality of the weld. The parts are classified into 3 categories namely, under melt, over melt, and beautifully welded. Using pre- and post-laser scan images Snow et al. [23] proposed an online CNN based flaw detection system to identify small and large surface defects. Grasso et al. [24] proposed an infrared imaging based in situ monitoring method for the MAM process. The system uses image processing techniques to detect unstable conditions by monitoring the process plume infrared images. Caggiano et al. [25] developed an online defect identification system for SLM based on image processing. A deep convolutional neural network model was used to classify the defects with 99.4 % accuracy. Akhil et al. [26] have developed an image processing method to predict the surface roughness parameters like S_a, S_q, and S_t during the MAM of Ti6AL4V. The raw images for analysis are captured using a digital microscope. Among various prediction models, Gaussian process regression was reported to have the maximum accuracy with an R^2 value of greater than 0.9. Kleszczynski et al. [27] used externally mounted vision sensors to capture high resolution images during the process. The perspective correction is performed through image processing and the method is projected as a proof of concept which could be used in future online defect detection systems. Abdelrahman et al. [28] proposed an image processing based optical flaw detection method. Here the powder bed is captured using DSLR cameras and the images are analysed to identify anomalies in power distribution after a laser scan. Even though these online methods are very promising, in-situ methods of inspection are very complex, demand high computational requirements, and are very expensive to set up. Also, such systems have limited capability to regulate the defects caused due to the inherent process mechanism like balling, stepping and corner inaccuracies. To achieve acceptable surface integrity, some post process finishing is often unavoidable. Image processing of MAMed components to analyse and perform post process finishing has not been explored much thus far. To the best of the authors' knowledge, the only work in this regard is by Caggiano et al. [29] who have developed a convolutional neural network (CNN) based model to predict the optimal parameter combination to perform laser polishing (LP) for the additive manufactured components. The CNN model receives input images from a stereo microscope with 8x magnification and gives the optimal LP parameter settings as the response. In this way, the developed system could automate the parameter selection for LP.

From the literature review, it was understood that the MAM process requires post-processing due to its inherent defects and the traditional methods for finishing have several limitations. In this regard, a relatively unexplored WEDP method is proposed in this study. Although surface integrity improvements through post-processing of MAM components were reported previously, not enough studies were conducted on the

use of image processing to enhance the corner profile accuracy. In this context, an image processing approach has been proposed to compute the minimal polishing depth for enhancing corner accuracy. The proposed method also gives an insight into the part allowances to be considered during the MAM process in the subsequent production batches.

3. Mechanism of WEDP

WEDP is a hybrid polishing process whose mechanism of material removal is controlled and repetitive low energy electric sparks. The electric sparks are generated between an electrically conductive metallic component and a thin metallic wire electrode[30, 31]. Material removal happens by virtue of the heat energy of discharge sparks which causes melting and vaporization of a thin surface layer [20, 32]. The surface unevenness of the MAM built component is selectively removed in this process to improve the corner accuracy, surface finish, and mechanical properties[33].

The depth of polishing is selected based on surface roughness parameter S_z and radial inaccuracy of the built corner. As illustrated in Fig. 1, the wire is traversed towards the workpiece in Y direction to find a minimum spark distance through a pre-programmed 'edge finder' module. The edge finder program stops the wire movement at the first instance of spark detection. This wire location is considered as zero reference coordinate in the Y direction. From this location, the wire is advanced in the Y direction at a distance equal to minimum polishing depth. Then, the part is polished by translating wire in the X direction all through the length of the surface. Unlike other electrical discharge processes, WEDP works in an extremely low energy regime since it is a polishing technique. WEDP process parameters are regulated to ensure that the discharge energy is low enough to precisely remove the required thin, rough layer of MAM built specimen.

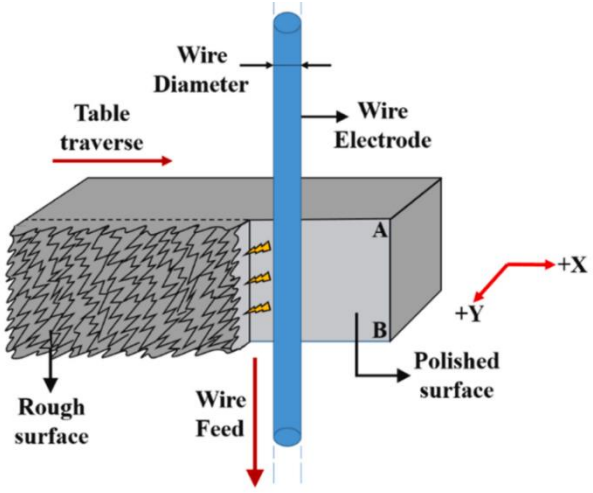

Fig. 1. Schematic of WEDP process [20]

4. Experimental Procedure

4.1 Material and experimental details

Ti6Al4V metallic powder is used for selective laser melting, due to the alloy's extensive industrial applications. The alloy is widely used in marine, chemical, biomedical and aerospace industries since it possesses excellent strength to weight ratio, biocompatibility, fatigue resistance and fracture toughness. The chemical composition of Ti6Al4V is given in Table 1. EOS M290 metal 3D printer is used to print the specimens in this study. The shape, dimensions (in mm) and built direction of the specimen is given in Fig. 2. The selected shape enables the corner accuracy studies for multiple angles. The specimen is built in the +Z axis direction. The printing takes place in an inert argon environment to prevent chemical reactions during the high temperature melting. The selected MAM and WEDP process parameters and levels are given in Table 2. Overall, 14 samples are printed in which hatch distance is varied in 3 levels, and laser power and scan speed are varied in 2 levels. An additional 2 experiments are conducted to study the effects of contouring and up-skinning.

Table 1. Chemical Composition of Ti6Al4V powder material

Element	Al	C	H	Fe	N	O	Ti	V
Wt. %	6.2	0.01	0.002	0.09	0.01	0.09	Bal	4

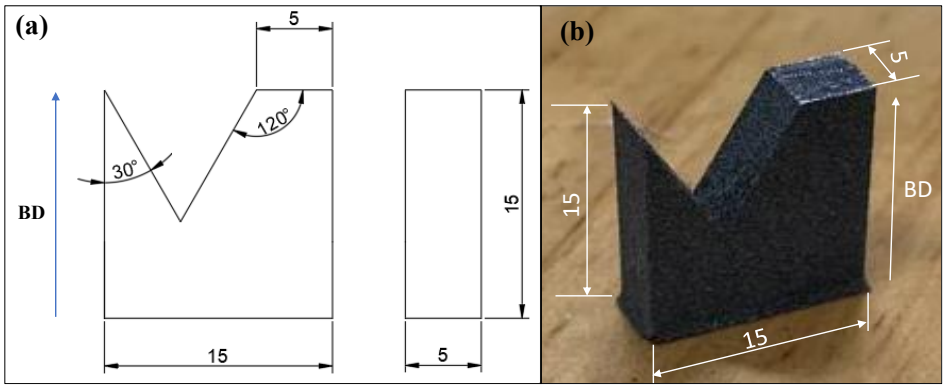

Fig. 2. (a) Dimensions (in mm) and build direction of the MAM specimen
(b) Image of the as-built Ti6Al4V MAM specimen

Table 2. Selected process parameters and its levels used for printing

MAM Parameters	Values	WEDP Parameters	Values
Layer thickness (μm)	30	Wire diameter (mm)	0.25
Laser Power (W)	200, 280	Wire feed rate (m/min)	3
Laser scanning speed (mm/s)	1250, 1500	Discharge current (A)	12
Hatch distance (μm)	0.14, 0.18, 0.22	Servo Voltage (V)	20
		Pulse on time, T_{ON} (mu)	10
		Pulse off time, T_{OFF} (mu)	10

An Electronica Ecocut wire electrical discharge machine is used to polish the MAM built specimens in this study. The machine has two standard finish cut settings with different energy modes. The lowest energy mode is chosen for the study since a predetermined rough layer is to be precisely removed from the surface. Deionized water with an electrical conductivity of ~20 μS/cm is used as the dielectric fluid in this study. Chemical contamination of the polished surface will thus be reduced compared to the hydrocarbon-based dielectric fluids. Due to its superior overall performance over uncoated wire electrodes, zinc-coated brass wire of 0.25 mm diameter is selected as the wire electrode [34, 35].

A Tobo make portable USB digital camera of 50 to 1000 × magnification is used to image the samples. The corner profile captured by the microscope is sent to a dedicated high-performance PC for further processing. The image processing and subsequent operations are performed using Matlab 2022a software. Surface roughness parameter (S_z) is measured using a Mitutoyo Surftest SJ-310 contact surface profiler. An AEP Nanomap1000 non-contact 3D surface profilometer is used to capture surface morphology and measure surface roughness parameters.

4.2 Methodology of image processing based corner accuracy detection

An image processing algorithm was designed, developed, and implemented to detect corner accuracy of MAM components. The raw image captured by the USB camera is pre-processed and enhanced to facilitate easier extraction of the required features. The relevant feature extracted in this case are the different corner profiles of the MAM built specimens. Fig. 3 shows the overall methodology of the proposed image processing-based corner accuracy detection system. The various steps involved in the image processing method are described as follows.

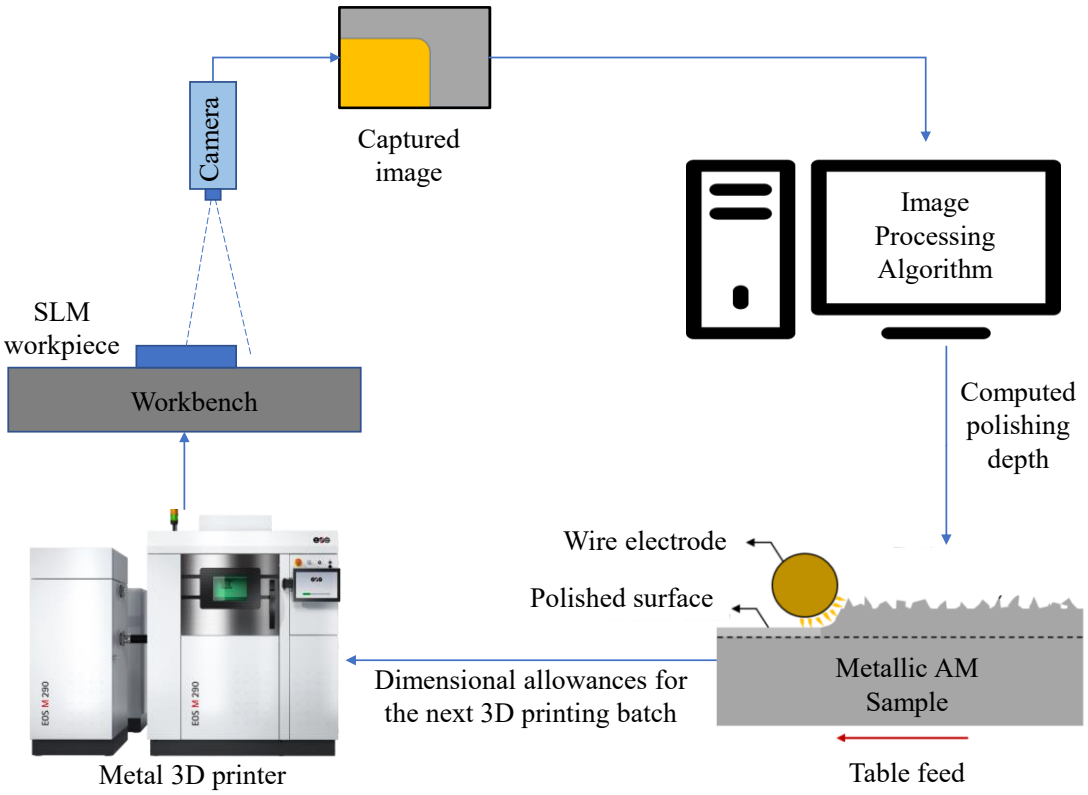

Fig. 3. Methodology of the image processing-based corner accuracy improvement system

Step 1: Capturing the raw image

Image acquisition is the first step in image processing. In this study, a USB camera is used to capture the raw image of the MAM built component. The camera captures the corner area of the specimen at a scale of 400 µm as shown in Fig. 4. The captured raw image in its initial state is too noisy to fetch any useful information from it. The image is sent to the integrated PC for further processing and enhancement.

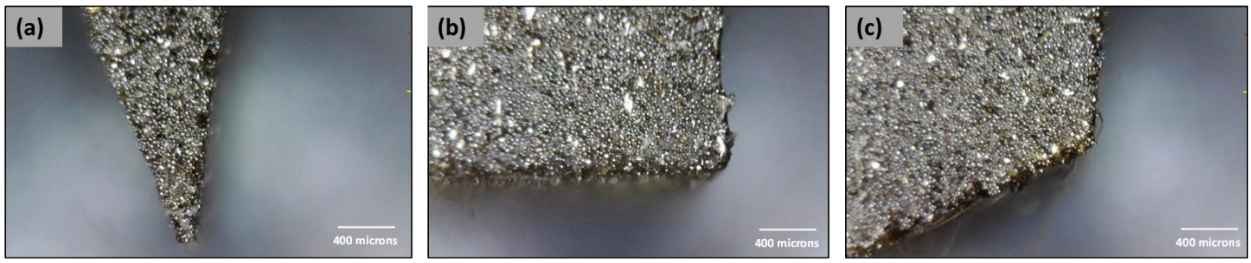

Fig. 4. Raw images of MAM as-built specimen for (a) acute (b) orthogonal (c) obtuse profile

Step 2: Greyscale conversion and background removal

The next step in image processing is grayscale conversion. In this step, the colored RGB image is converted to a monochrome grayscale image. The greyscale image would contain pixel values that represent the luminance of the respective pixel. The metallic part is expected to be brighter than the background due to its higher reflective nature. To further distinguish between the metallic surface and the background, contrast enhancement through histogram equalization is performed. Histogram equalization is used to distribute the pixel intensities uniformly so that the global contrast is improved. This is usually done when the relevant part of the image is difficult to distinguish from its background. Further, background correction and background subtraction are performed using the Image Processing Toolbox to separate the metallic subject from its background.

Background subtraction or foreground detection is a technique used to detect objects of interest that are in the foreground. The idea is to identify the difference between a frame of reference and the current frame. A frame difference method is employed to perform foreground detection.

Mathematically, the model can be expressed as

$$|Frame_i - Frame_{i-1}| > Threshold \tag{1}$$

$$Region\ of\ interest = \begin{matrix} unchanged \\ 0 \end{matrix} \quad \begin{matrix} (|Frame_i - Frame_{i-1}| > Threshold\ ) \\ otherwise \end{matrix} \tag{2}$$

Where the $Frame_i$ represents the input frame and $Frame_{i-1}$ represents the background frame. Thus, for any changes greater than the threshold limit in the input image with respect to the background frame, the foreground detection model detects the foreground and retains the pixel values for the foreground subject. The model assigns a value of 0 to every other pixel except the subject of interest. The computational block diagram of the frame difference method is shown in Fig. 5.

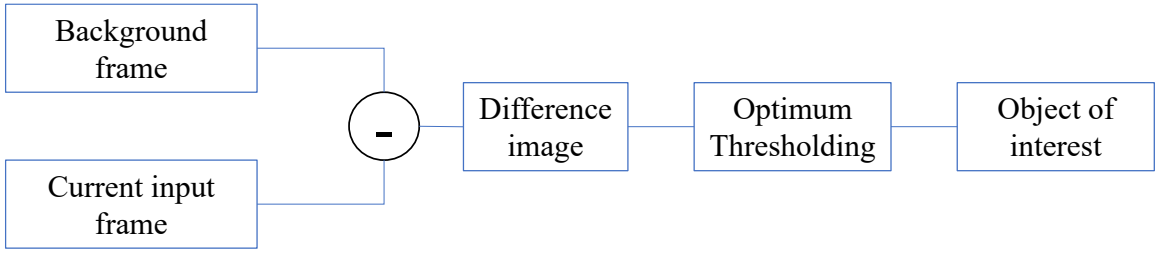

Fig. 5 Frame Difference Method

The output image from the foreground detection method is thus just the subject of interest in a black background. This is post processed to form a binary image in the pre-processing stage so that the boundary

coordinates can be separated easily. The data flow diagram of a typical background subtraction program is given in Fig. 6.

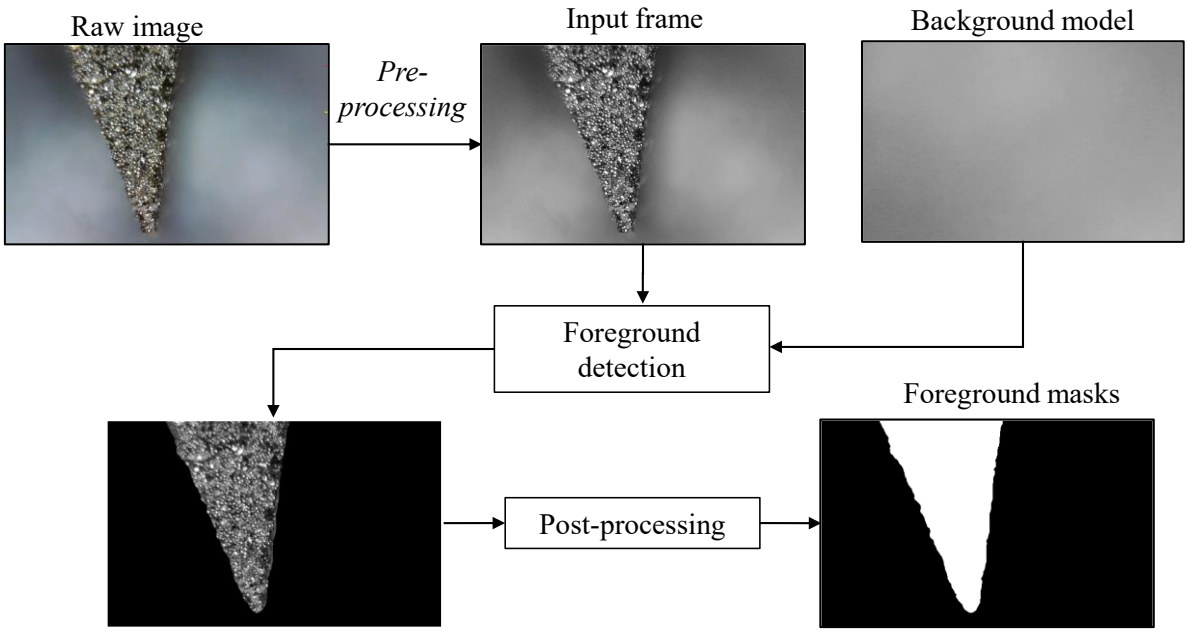

Fig. 6 Data flow diagram of a typical background subtraction program

Step 3: Binary conversion

Binary conversion is the step where a greyscale image is converted to a binary image based on a threshold pixel luminance value. Unlike a greyscale image, a binary image will contain only either black or white pixels. All the pixels above the threshold value are assigned a value of 1 (which is white in colour) and those below the threshold are assigned a value of 0 (which is black). Due to its greater luminance, the major portion of the metallic surface is expected to be white, with the background being black.

Step 4: Filling and morphological operation

Even after the binary conversion, there will be black spots/regions surrounding white metallic region. A filling operation fills all these holes in a binary image. Morphological operations like dilation and erosion are performed next. Dilation is performed to smoothen the binary image boundaries and also to bridge the gaps. On the contrary, an erosion operation eliminates noises by removing the smaller white pixel areas. An external pixel set in the form of a structural element interacts with the binary image to perform the morphological operations. A disc shaped structuring element of radius 3 pixels is used in this case. Fig. 7 shows the binary pixel matrix of the disc shaped structural element of radius 3. The pixel value '1' defines

the active neighbourhood elements of the operator. Erosion followed by dilation is the sequence of morphological operation used in this study.

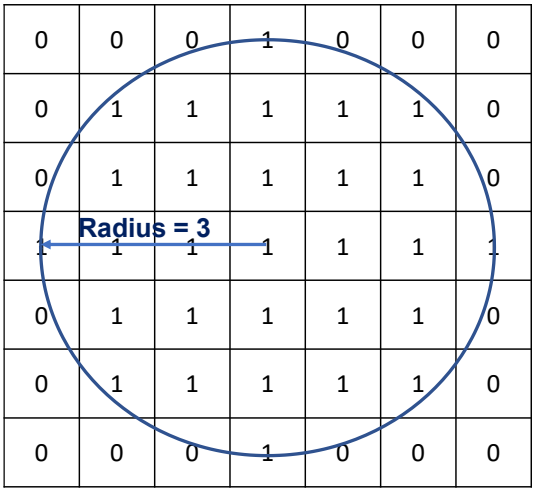

Fig. 7. Pixel matrix of disc shaped morphological operator

Let A be the binary image and B be a structural element. Then, erosion operation is mathematically expressed as

$$A\Theta B = \bigcup_{b\epsilon B} A_{-b} \tag{3}$$

Where A_{-b} represents the translation of the structural element B over the image A. During erosion operation, the pixel set B is translated through A with respect to its origin (at centre of B), and only those pixels of A are retained which can enclose B entirely. Every other pixel of A is eroded to 0.

Dilation operation of B on A is given by

$$A \oplus \mathrm{B} = \bigcup_{b\epsilon B} A_b \tag{4}$$

Where A_b represents the translation of B over A. During the operation, the origin of B moves with respect to all pixels in A thereby enlarging and smoothening the original image. The morphological operators are thus used to eliminate the imperfections and smoothen the boundaries in an image. Fig. 8 shows the binary images after morphological operation.

Fig. 8. Binary images of MAM as-built specimen after morphological operation for (a) acute (b) orthogonal (c) obtuse profile

Step 5: Image segmentation

The coordinate of the white region boundaries is extracted next. Edge detection is performed through a Sobel edge detection algorithm. Ideally, it is expected that at this point there will only be 2 regions; one white region representing the MAM built metallic part and a black region representing its background. However, due to the background noises, there may be other white pixel regions within the black pixel region. These regions will be of smaller dimensions compared to the main region. Thus, to filter out these background noises, only the coordinate data of the largest white area is taken, and the remaining are disregarded.

Step 6: Edge profile extraction

A curve is plotted through the extracted coordinates to reveal the separation boundary between the MAM build component and its background. The remaining operations are performed on this curve to compute the corner inaccuracy and radial error.

4.3 Computation of polishing depth based on corner profile

The methodology to compute the polishing depth from the extracted edge profile is described in this section. Firstly, the corner profile is separated from the closed curve by eliminating the irrelevant regions of the curve. Next, linear regression models are fit from both surfaces by taking the average coordinates of 3 locations separated by 50-pixel coordinates. From Fig. 9, the coordinates of point P correspond to the average coordinate values of the first 50 data points of the curve in the x direction. Point Q is obtained by averaging the next 50 points and so on. The points thus obtained in both the surfaces are denoted by P, Q, R and S, T, U respectively for all the profiles as shown in Fig. 9. When extrapolated, both these linear curves intersected at the theoretical corner point A. The radial correction factor is the minimum distance from the theoretical corner point A to the actual corner (denoted by B) profile of the specimen, denoted by δ_r. The minimum polishing depth, denoted by d_p is computed by the following equation

$$d_p = \delta_r \, sin\left(\theta/2\right) \tag{5}$$

where d_p is the polishing depth, δ_r is the radial correction factor and θ is the corner angle.

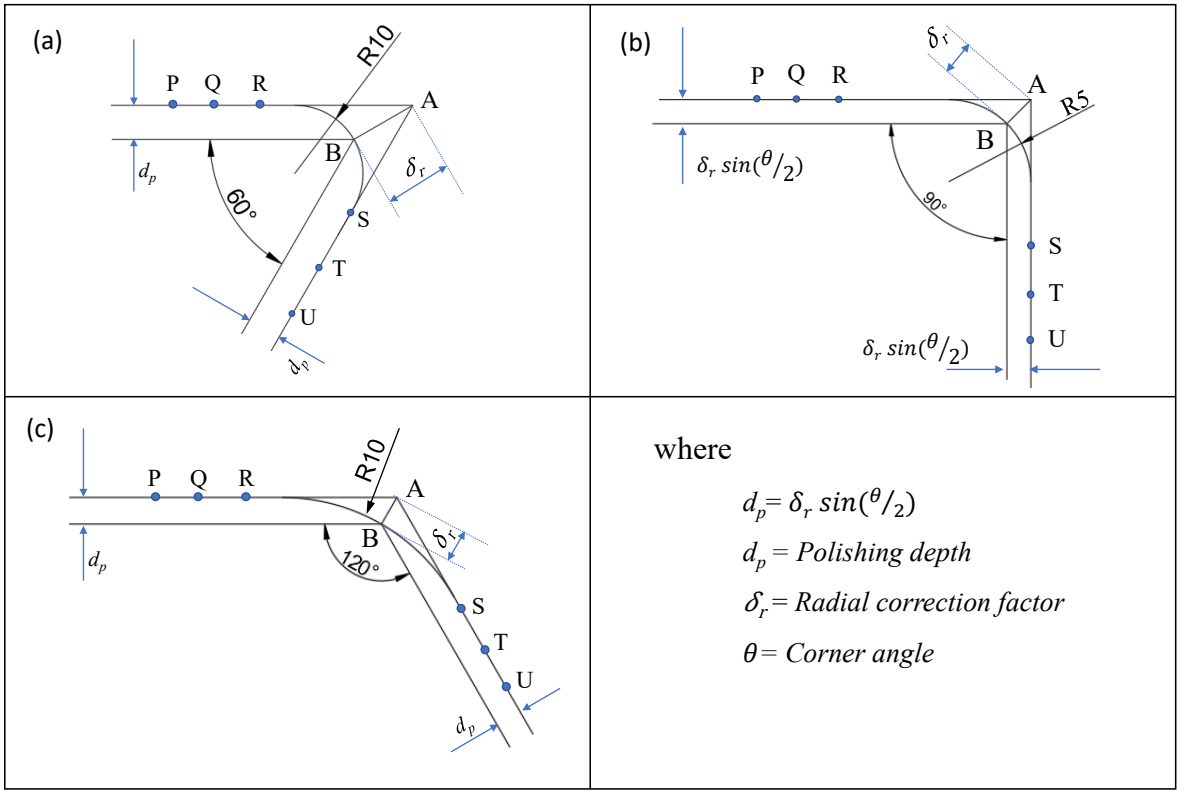

Fig. 9. Calculation of polishing depth from as-built MAM specimen images

This calculation holds good for any type of corner angle whether it is orthogonal, acute or obtuse as shown in Fig. 9 (a), (b), and (c) respectively. Fig. 10 shows the extracted corner profiles and their deviation from the required shape. The red marker (point A shown in red dot) indicates the ideal corner coordinates, and the blue marker (point B shown in blue dot) shows the actual corner coordinates.

The MATLAB codes for profile extraction and computation of radial correction are given in Appendix.

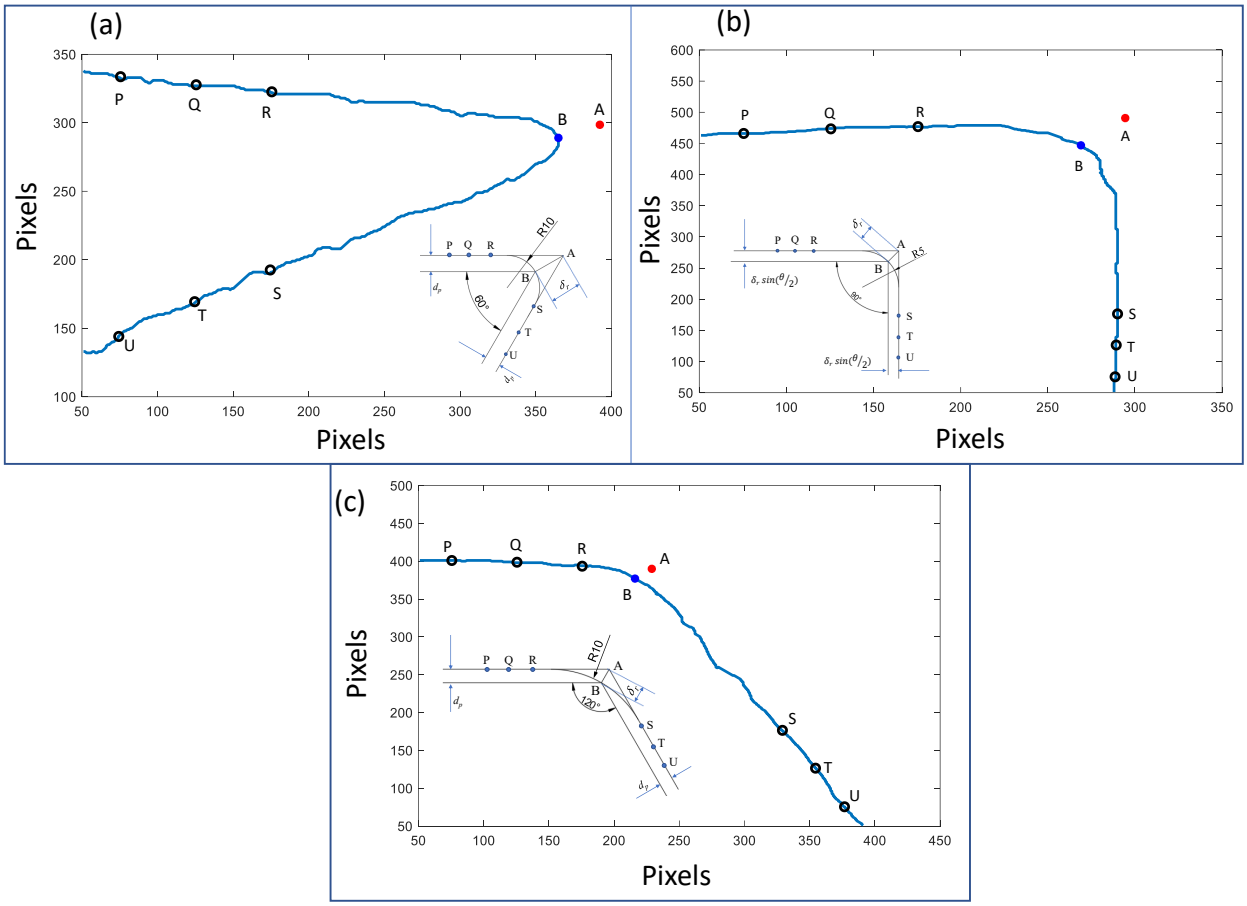

Fig. 10. Extracted profile of as-built MAM specimens for (a) acute (b) orthogonal (c) obtuse angle profiles

Lastly, consider a surface having 2 corners at each end. Based on the calculation described earlier, different polishing depths are recommended to correct the inaccuracies at each corner. The final polishing depth of the surface is the higher value among these two calculated depths. Fig. 11 summarizes the overall methodology of calculating the final polishing depth for WEDP based on the corner inaccuracy.

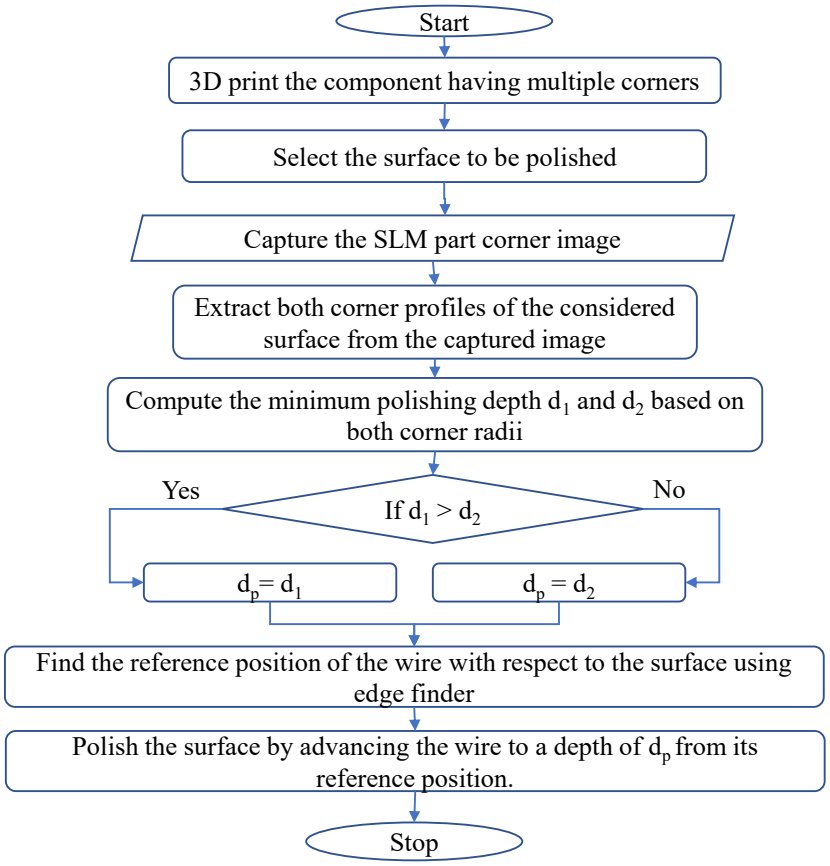

Fig. 11. Flowchart of the polishing depth computation

5. Results and discussion

Table 3 shows the extracted profile information of the as-built MAM specimens. For each of the 14 components, corner profile inaccuracies and appropriate polishing depths are computed separately for acute, orthogonal and obtuse angle configurations. It was observed that the average radial deviation from the ideal corner coordinates to the actual profile is 212.4 µm, 117.6 µm, and 68.8 µm for acute, orthogonal, and obtuse profiles respectively. This can be explained since, the lower the corner angle, the higher will be the dimensional deviation for MAM fabricated components. This agrees with the earlier studies which also reported difficulty in achieving sharp corners using the MAM process [3].

The effects of process parameters on the radial correction factor are given in Fig. 12 for different corner profiles. Fig. 12 (a), (b), and (c) corresponds to the acute, orthogonal and obtuse profiles respectively. The plots are generated by varying the parameter under consideration while keeping the other parameters constant. Hatch distance of 0.18 µm, laser power of 200 W and a scan speed of 1250 mm/s are the selected constant parameter values. From the figure, higher hatch distance, laser power and laser scanning speed resulted in greater inaccuracies irrespective of the corner angle. At higher laser power, the thermal energy

per volume is high resulting in a larger melt pool. Such a setting makes it difficult to achieve accurate corners since a precise melt area is required to achieve near zero corner radii. Also, the elevated scan speed can lead to inaccurate scanning at the corners due to the sudden change in the scan direction. Lesser hatch distance has led to a more accurate corner profile. This is because a larger hatch distance results in the reduced overlap between adjacent melt tracks, which may lead to the porous structure and part defects. This is especially critical in the case of an acute angle since the profile to be machined is very slender and higher in aspect ratio than the other two angles.

Table 3. Computed polishing depth for various angular features from as-built MAM fabricated specimen images

S. No	Hatch distance (μm)	Laser power (W)	Scan speed (mm/s)	Contour	Up-skin	Orthogonal ($\theta = 90^O$)		Acute ($\theta = 30^O$)		Obtuse ($\theta = 120^O$)	
						δ_r (μm)	d_p (μm)	δ_r (μm)	d_p (μm)	δ_r (μm)	d_p (μm)
1	0.14	280	1250	Off	Off	95.5	67.5	155.3	40.2	54.9	47.5
2	0.18	200	1500			115.9	81.9	325.1	84.1	58.6	50.7
3	0.14	200	1500			64.8	45.8	95.3	24.7	56.4	48.8
4	0.18	280	1250			89.5	63.3	363.7	94.1	63.4	54.9
5	0.14	200	1250			53.3	37.7	83.4	21.6	23.4	20.3
6	0.18	280	1500			104.0	73.6	180.5	46.7	47.3	40.9
7	0.14	280	1500			190.9	135.0	230.0	59.5	118.6	102.7
8	0.18	200	1250			75.6	53.4	105.7	27.4	47.9	41.5
9	0.22	280	1250			71.8	50.8	191.7	49.6	44.9	38.9
10	0.22	200	1250			91.6	64.8	126.4	32.7	87.6	75.9
11	0.22	280	1500			63.4	44.8	301.2	78.0	59.3	51.4
12	0.22	200	1500			145.9	103.2	311.9	80.7	34.3	29.7
13	0.14	280	1250	On	Off	341.7	241.6	411.3	106.5	85.3	73.9
14	0.14	280	1250	On	On	141.9	100.4	76.2	19.7	63.5	55.0

δ_r= radial correction factor, d_p= computed polishing depth

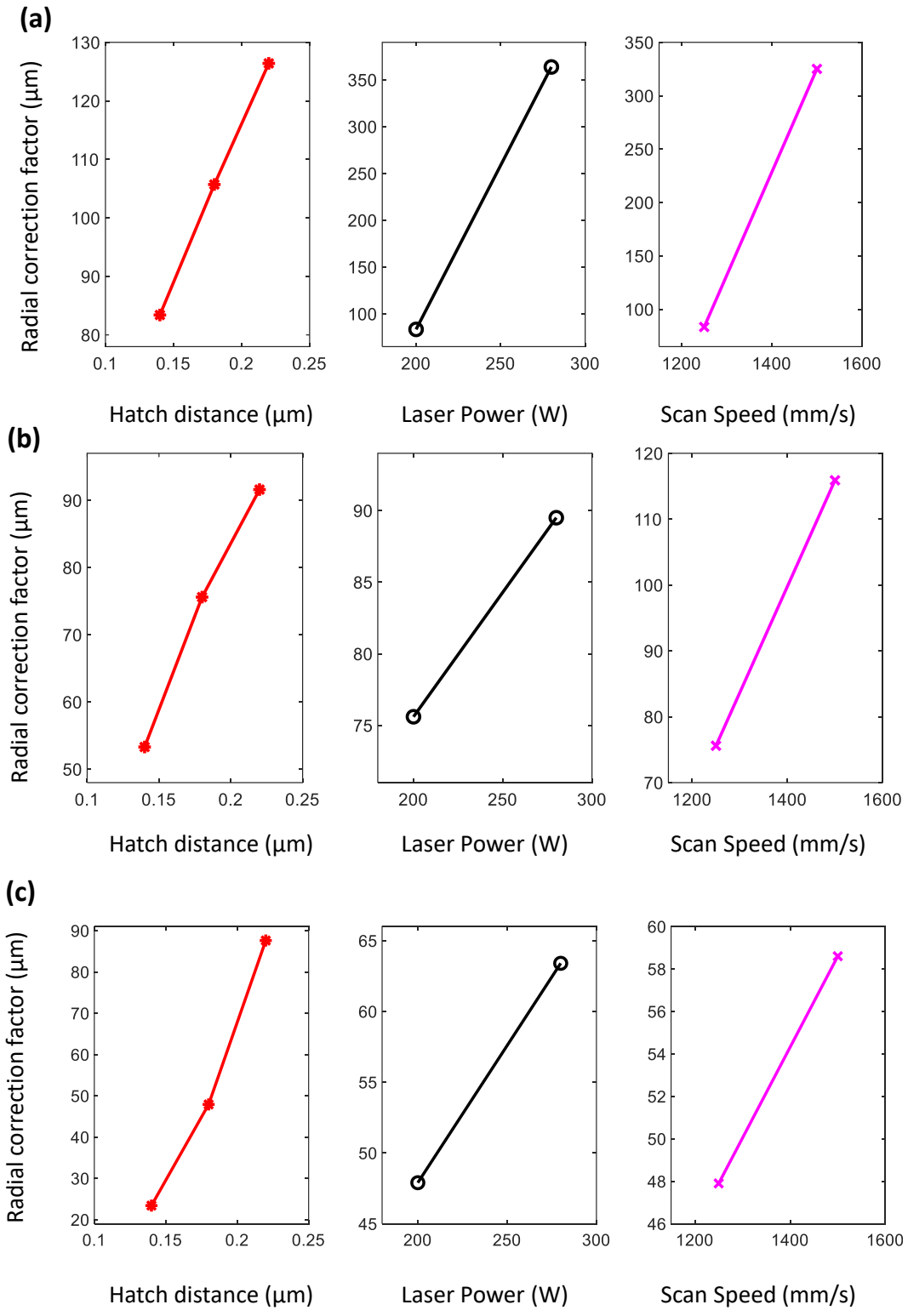

Fig. 12 Effects of process parameters on radial correction factor for (a) acute (b) orthogonal (c) obtuse profile

5.1 Corner accuracy improvements after WEDP

The corner accuracy has been significantly improved after WEDP as shown in Table 4. The average improvement in radial correction factor after polishing is 80.7 %, 77.3 % and 85.4 % for orthogonal, acute and obtuse respectively. Fig. 13 shows the comparison of radial correction factors in MAM fabricated components before and after WEDP for multiple angles.

Table 4. Improvement in the corner accuracy after WEDP

S. No.	Orthogonal ($\theta = 90^O$)			Acute ($\theta = 30^O$)			Obtuse ($\theta = 120^O$)		
	δ_r (As-built)	δ_r (WED polished)	% Improvement	δ_r (As-built)	δ_r (WED polished)	% Improvement	δ_r (As-built)	δ_r (WED polished)	% Improvement
1	95.5	2.0	97.9	155.3	31.05	80.0	54.9	4.9	91.2
2	115.9	10.5	90.9	325.1	41.04	87.4	58.6	11.8	79.9
3	64.8	28.7	55.7	95.3	54.63	42.7	56.4	6.0	89.3
4	89.5	18.4	79.5	363.7	27.31	92.5	63.4	11.7	81.6
5	53.3	42.8	53.3	83.4	7.15	94.1	23.4	6.1	94.5
6	104.0	9.5	90.9	180.5	13.77	92.4	47.3	13.8	70.9
7	190.9	3.0	98.4	230.0	99.45	56.8	118.6	3.2	97.3
8	75.6	10.9	85.6	105.7	20.88	75.0	47.9	12.8	81.1
9	71.8	9.4	86.9	191.7	33.525	82.5	44.9	15.8	64.9
10	91.6	20.3	61.8	126.4	86.67	31.4	87.6	0.7	99.2
11	63.4	6.4	89.9	301.2	45.54	84.9	59.3	6.8	88.5
12	145.9	15.0	89.7	311.9	70.515	77.4	34.3	4.5	87.0
13	341.7	59.0	82.7	411.3	23.49	94.3	85.3	20.2	76.3
14	141.9	46.7	67.1	76.2	6.345	91.7	63.5	3.6	94.3

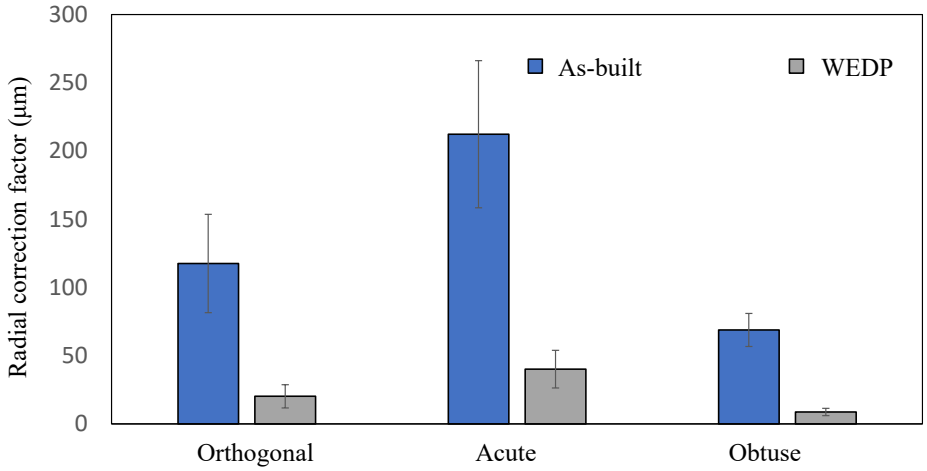

Fig. 13 Corner accuracy comparison of as-built and WEDP specimens

Fig. 14 shows the raw image and enhanced binary images for all the angles considered. Here, Exp. No. 8, Exp. No. 11 and Exp. No. 7 is considered to demonstrate the corner accuracy improvements for acute, orthogonal, and obtuse angles respectively. It can be clearly noticed that, in comparison to the as-built MAM specimen profiles, the polished profiles are observably very smooth with accurate corners. This is because of the precise removal of the computed polishing depth from the surface using WEDP.

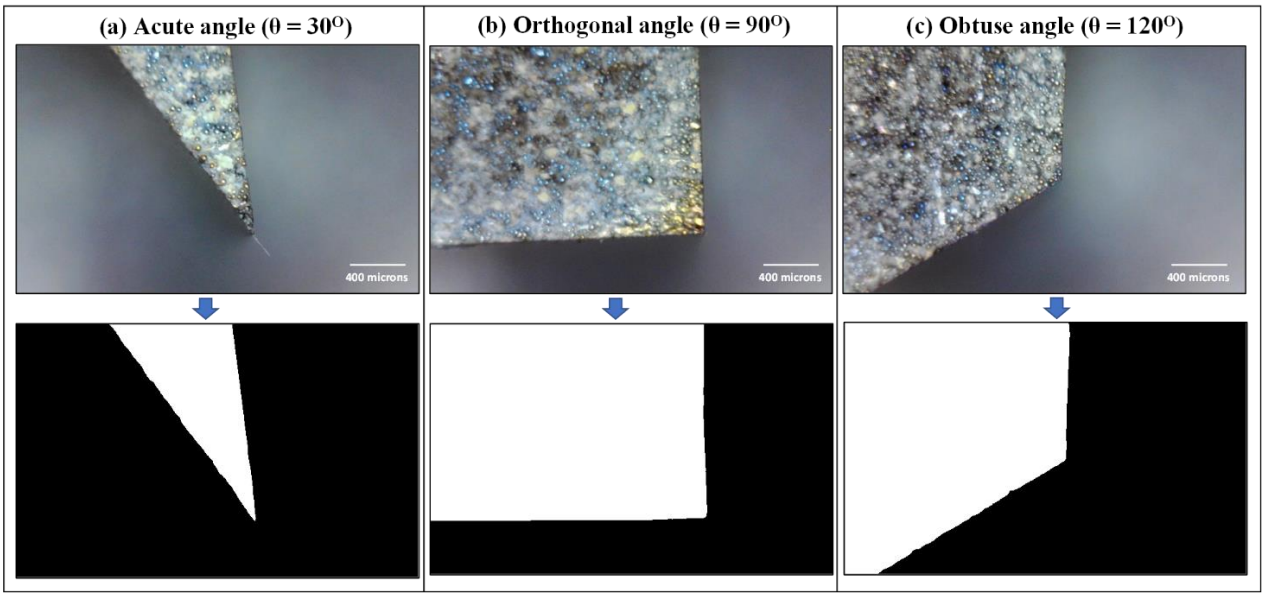

Fig. 14 Binary enhanced images of WEDP processed MAM specimen for (a) acute (b) orthogonal (c) obtuse profile

Wire EDM process is already proven to be extremely capable of producing sharp and accurate corners [36]. Some of the reported limitations of wire EDM like wire bending and the presence of a recast layer are not present during WEDP. This is due to the lower discharge energy associated with WEDP. Also, unlike the wire EDM rough cut operation, here the wire electrode is not cutting through the material, to cause unbalanced forces from multiple directions resulting in wire vibration, bending, and bowing. Rather, the wire flushes through the periphery of the profile with minimal spark energy, thus minimizing the resultant force acting on the electrode. Thereby the wire electrode can maintain its intended position throughout the polishing operation. The presence of a recast layer is also reported to limit the surface quality of the EDM machined surface [37]. However, in WEDP there is no deposition of resolidified molten materials back into the machined surface[20]. This is due to the lesser material removal combined with the higher dielectric flushing rate. This implies that WEDP leaves negligible recast layer on the polished surface which helps to maintain the profile accuracy. Additionally, unlike conventional EDM, the effect of tool wear on corner accuracy is also prevented in WEDP by the continuous feeding of fresh wire into the machining zone.

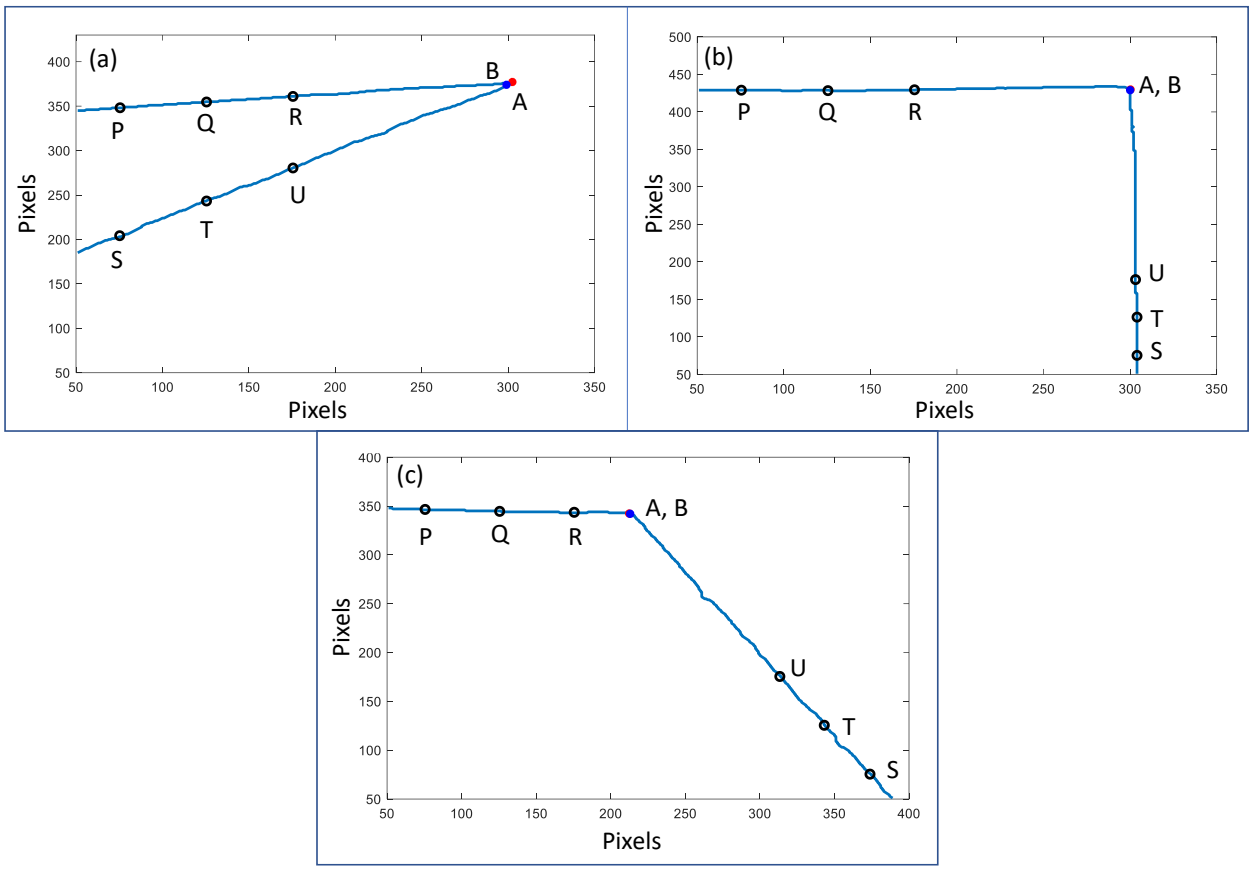

Fig. 15 Extracted profile of WEDP finished MAM specimens for (a) acute (b) orthogonal (c) obtuse angle profiles

As opposed to the extracted profiles of as-built MAM fabricated specimens (Fig. 9), the deviation of actual to the ideal/expected corner coordinates are negligible after WEDP, which is evident from Fig. 15. From Fig. 15 (a), it can be observed that the actual (denoted by blue marker) and expected (denoted by the red marker) corner coordinates are very close to each other in the case of acute angled profile. In the case of orthogonal and obtuse angles, actual and ideal coordinates are almost coinciding which implies a perfect corner accuracy with a negligible edge radius as shown in Fig. 15 (b) and Fig. 15 (c). The average deviation from the expected corner coordinates is 5.43 µm, 17 µm, and 27.65 µm for obtuse, orthogonal and acute corners of WEDP-finished MAM fabricated components. Like the as-built case, the deviations increase with a decrease in corner angle for WEDP processed samples also. The marginal increase in acute-angled corner inaccuracy for polished MAM fabricated components is due to the reversal of wire traverse direction from the corner point. The traverse of the wire electrode decelerates to an absolute halt at the corner and then it goes back to trace the other surface. The wire velocity is thus not uniform throughout the profile. This extended wire halt duration could have resulted in additional material removal from the corner point resulting in a higher inaccuracy compared to the orthogonal and obtuse polished corners.

5.2 Surface integrity analysis of polished specimens

The inherent roughness of the as-built MAM components is attributed to surface unevenness imparted by multiple overlapping melt tracks, layer by layer nature of manufacturing, and the presence of partially melted powder particles on the surface. Additionally, the surface finish is influenced by balling defects and stair stepping in the case of vertical, curved, and inclined surfaces. Since MAM is a thermal process, the induced residual stresses can cause micro-cracks which can also deteriorate the surface quality. In this study, the roughness parameter R_z is measured on horizontal, vertical, and inclined surfaces and the average values are calculated for each specimen.

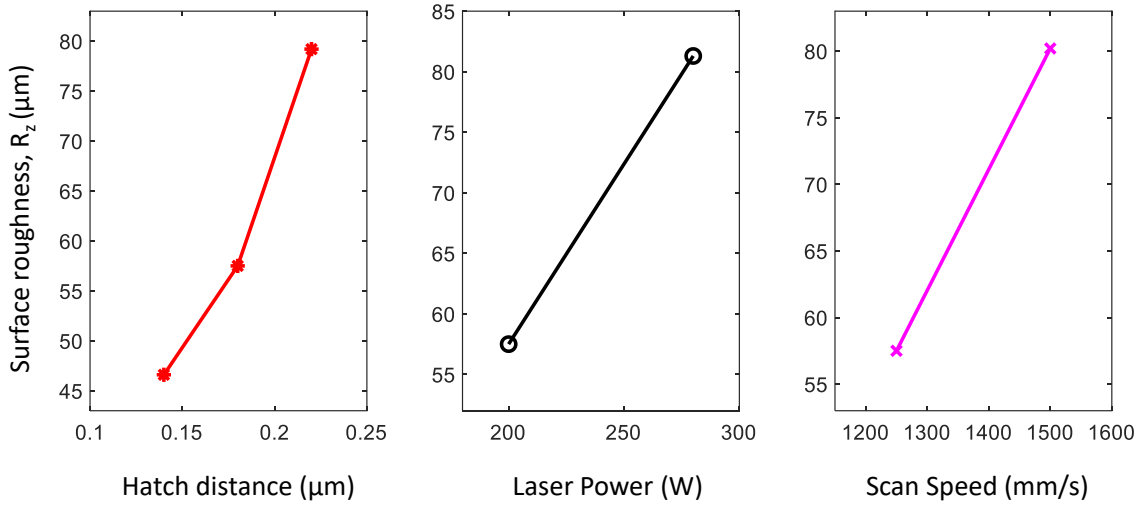

Fig. 16 Main effects plot of surface roughness

Fig. 16 shows the main effects plot for surface roughness (R_z) of as-built MAM fabricated samples. The better finish is observed at lesser hatch spacing since it ensures proper overlap of adjacent melt tracks thereby minimizing the presence of unmelted/partially melted powder particles. Also, higher laser power increases the melt pool dimension, and it causes splashing leading to balling effects which result in a rougher surface. The surface roughness (R_z) of MAM fabricated components is reported to be minimal at lesser scan speeds [38]. At higher scan speeds, the melt track dimension narrows down leading to improper melt track overlapping. This is the reason for an improved surface roughness at lower scan speeds.

Significant improvements in surface roughness R_z are observed after polishing as shown in Fig. 17. The average reduction in R_z after WEDP is observed to be 86.4 %. During WEDP, the irregular peaks are removed by melting and vaporization by sequence of discharges leading to sparks and the polished surface is thus covered with several shallow micro sized craters.

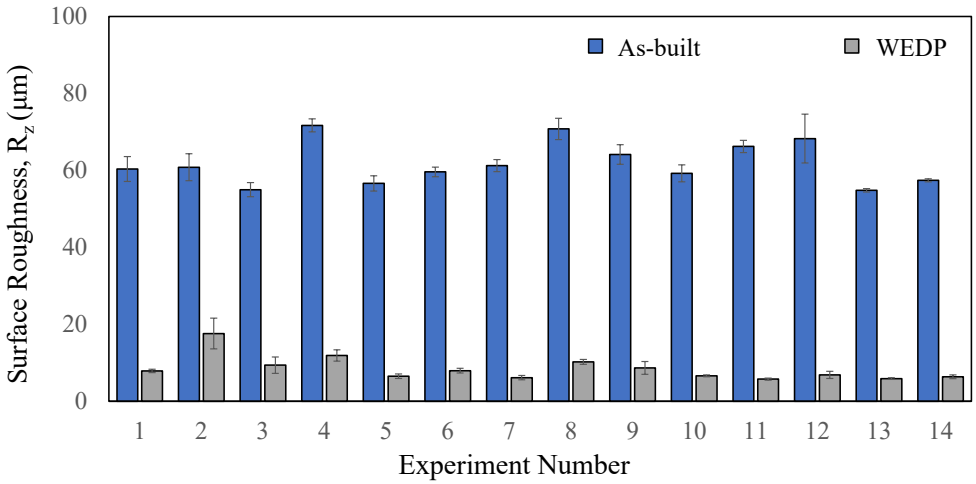

Fig. 17 Surface roughness improvements after WEDP

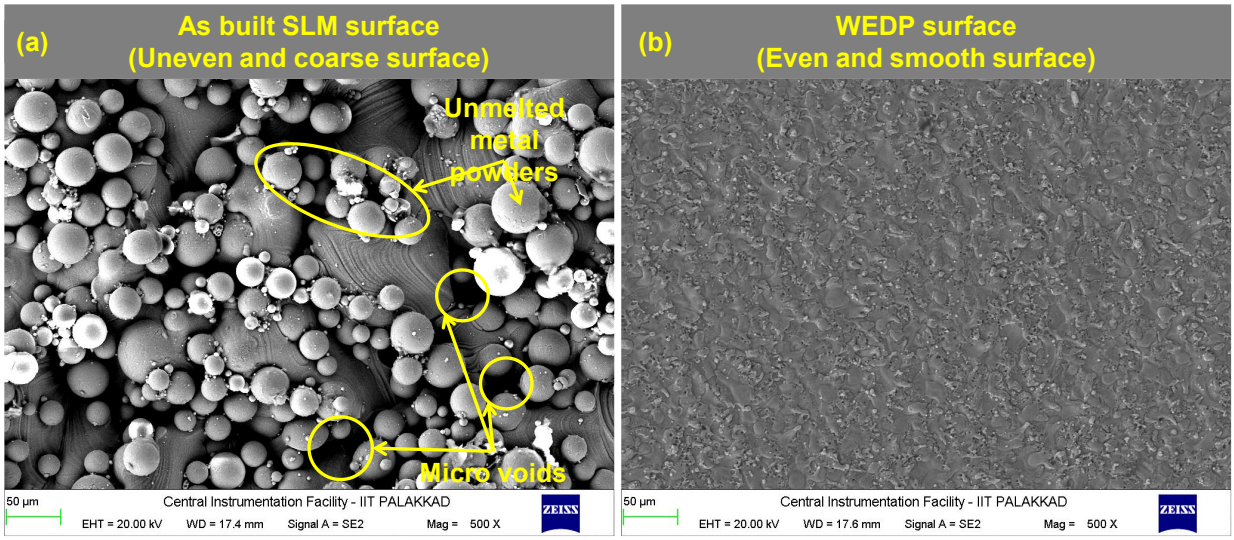

Fig. 18 Microstructural analysis of MAMed component (a) before and (b) after WEDP

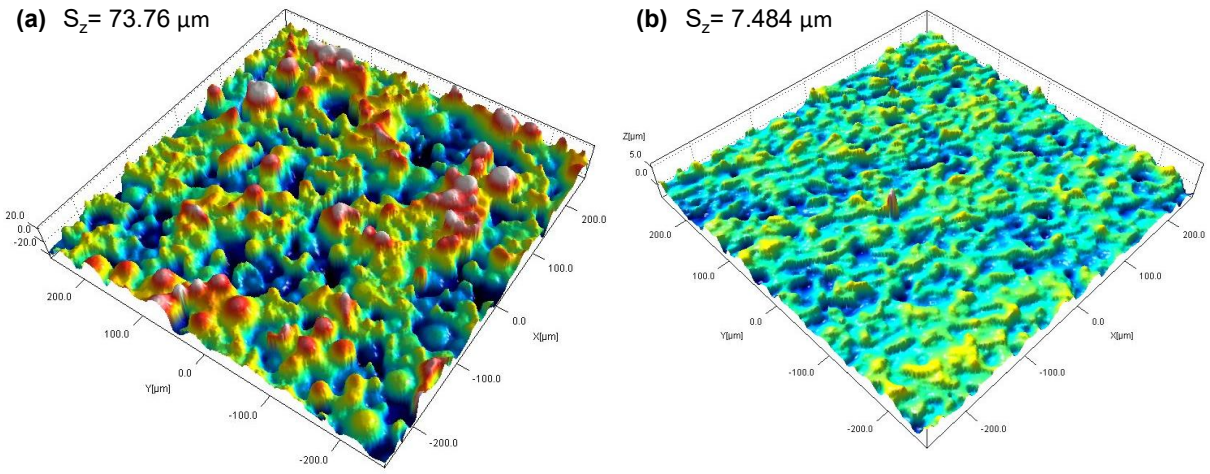

Fig. 19 Surface morphology comparison of MAMed component (a) before and (b) after WEDP using non-contact 3D profilometer

SEM images were captured using a Zeiss Gemini FESEM with 100 X magnification. The as-built samples are observed to be uneven and wavy with the presence of unmelted metallic powder particles as seen in Fig. 18 (a). The waviness is associated with the layer-by-layer manufacturing mechanism of MAM fabricated components. Also, several micro voids can be seen over the surface. These voids are associated with the lack of melting during the laser scan. It can be attributed to an insufficient overlap of adjacent melt tracks, which may be because of higher hatch spacing or lesser melt track width. This can also happen between layers when the melt pool is not deep enough to melt the entire powder layer. In comparison to the as-built surface, the WEDP finished surface looks very even, uniform and smooth as seen in Fig. 18 (b). The surface waviness and peaks are removed by controlled repetitive low energy discharge sparks during WEDP. As the operation takes place in a low energy regime, solidification and deposition of molten material back to the polished surface are also minimal. Therefore, undesirable features like craters and globules, which are usually the characteristic features of electric discharge machined surfaces are also absent. Non-contact 3D profilometer images are also used to demonstrate the improvements in surface morphology after WEDP. From Fig. 19, it can be observed that the as-built MAM fabricated components are having deep valleys and high peaks compared to the polished surfaces. The roughness parameter S_z obtained from the 3D profilometer is also observed to be significantly lesser after WEDP as compared to the as-built condition. For the case considered, the surface roughness (S_z) is reduced by 89.8 % after WEDP.

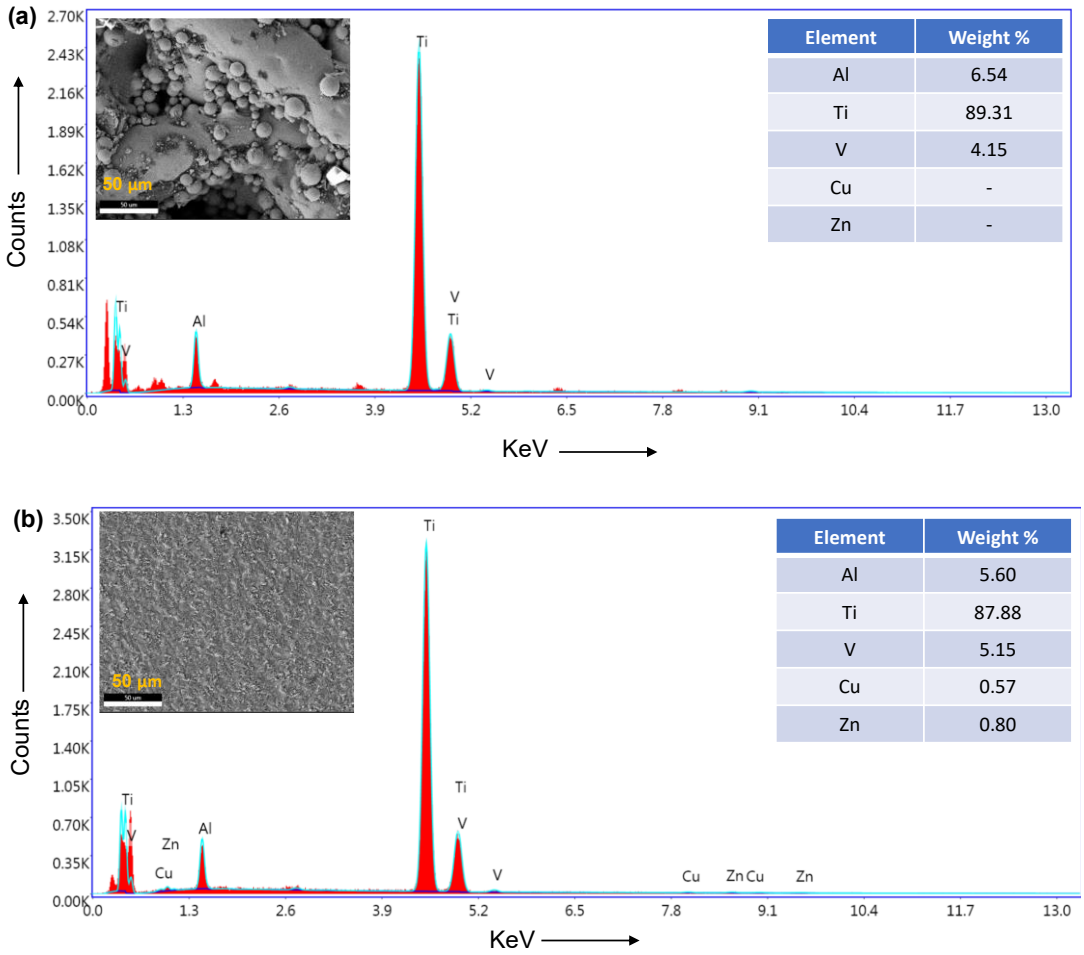

Fig. 20 EDS analysis of MAM fabricated component (a) under as-built condition (b) after WEDP

Wire EDM is reported to cause undesirable elemental migration between electrodes during the machining. When a zinc coated electrode is used as the wire material, considerable traces of zinc and copper were observed on the workpiece after wire EDM. Minimizing zinc contamination is extremely critical, especially for biomedical applications. Energy dispersive spectroscopy (EDS) analysis was performed to see the elemental migration from the wire electrode to the surface of the workpiece during WEDP. Unlike in the case of wire EDM, since a very low energy spark is used to polish the surface, the amount of material melted from wire electrodes is extremely less during WEDP [39, 40]. Thus, only a negligible amount of Zn and Cu are observed on the polished surface as shown in Fig. 20. 0.57 weight % of Cu and 0.80 weight % Zn are observed after WEDP which is comparatively less with respect to the overall composition. The WEDP process is thus proved to be capable of polishing MAMed components without any significant alteration to the elemental composition. Similar results were obtained for all the polished specimens.

5.3 CAD modelling of MAM specimens with polishing allowance

In an industrial production scenario, the dimensional deviation after WEDP may not be acceptable even though the resultant components have superior profile accuracy. In this case, for both dimensional and corner profile accuracy, the STL format CAD drawing should be revised for the subsequent production batch based on the computed polishing depths. The proposed image processing approach can be extended to a closed loop process control by incorporating the polishing allowances into the actual CAD model dimensions for the subsequent batch of production. Therefore, from the next batch onwards the required dimensions are obtained after WEDP as prescribed in the actual CAD model. A schematic showing the strategy for incorporating the allowance is depicted in Fig. 21. The capability of the strategy has been demonstrated using Exp. No. 1 (Table 3) as the test case.

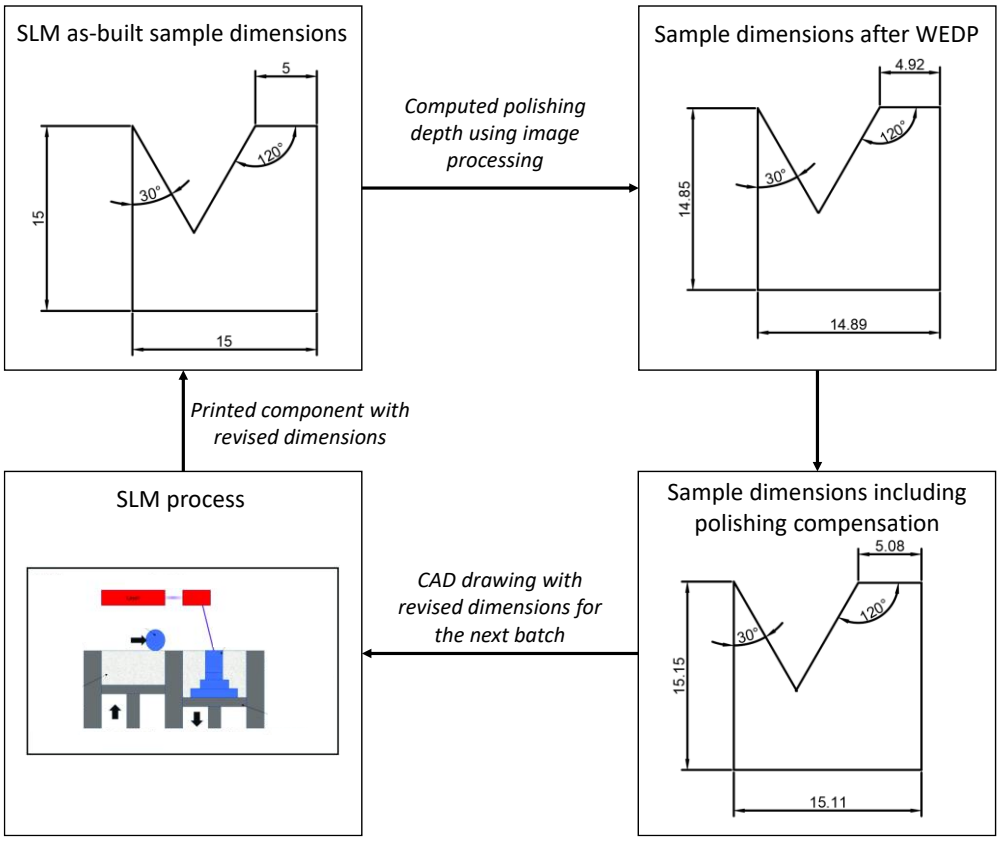

Fig. 21 Methodology for incorporating polishing allowance

6 Conclusions

The present study proposed an image processing approach for improving the dimensional accuracy of metal additive manufactured components using WEDP. The salient conclusions from the work are presented as follows.

1. An image processing methodology has been developed to extract the corner profiles from a MAM specimen to calculate the angular profile deviation from the ideal profile. The polishing depth to improve the corner edge is calculated based on the radial correction factor. Corner accuracy of MAM build components was observed to be very less with an average deviation of 212.4 μm, 117.6 μm, and 68.8 μm for acute, orthogonal and obtuse angles respectively.
2. An improvement in the radial error of 80.7 %, 77.3 % and 85.4 % was reported for orthogonal, acute and obtuse angled corners respectively. After WEDP, the average deviation has reduced to 5.43 μm, 17 μm, and 27.65 μm for obtuse, orthogonal and acute profiles. Thus, WEDP was found to be a promising polishing process to improve corner accuracy.
3. A significant surface roughness (S_z) reduction of 86.4 % is observed after WEDP of MAMed components. On average, WEDP has reduced the surface roughness (S_z) of MAMed components from 61.86 μm to 8.41 μm.
4. Surface morphology of the MAM samples is also improved after WEDP. The waviness and irregularities over the surface have been removed and the micro pits/voids present in the as-built samples were eliminated by WEDP. EDS analysis showed a negligible amount of Zn (0.57 wt. %) and Cu (0.8 wt. %) present over the finished surface.
5. Finally, a strategy to modify the CAD model dimensions based on the computed polishing depth has also been proposed for the subsequent batches of printing.

Though the study has tremendous potential to transform the post-processing of MAM components, the proposed method still demands manual imaging. Also, the polishing depth computation is now solely based on corner angles. However, there can be other features that influence the polishing depth as well, like depth of surface defects, which are not included in the scope of this study.

As a future work, autonomous in-situ imaging of MAM components can be implemented by installing a suitable camera within the build chamber. An image processing based surface defect identification model shall also be integrated to such an online system to incorporate the effects of surface defects too. To improve upon the image processing capabilities, machine learning models like deep convolutional neural networks (CNN) can be employed in place of the existing foreground detection and image segmentation for trainability and robustness. In addition, the strategy can be validated on multiple MAM and WEDP machines.

Appendix

The MATLAB code for profile extraction and computation of radial correction

```
%% extracting the edge profile of specimen
[B,L] = bwboundaries(bism,'noholes');
[max_size, max_index] = max(cellfun('size', B, 1));
curve=B{max_index};

%% remove first and last path
j=1;
for i=1:length(xraw)
if curve(i,1)> 50 && curve(i,2)> 50
    new_c(j,:)=curve(i,:);
    j=j+1;
end
end
plot(new_c(:,1),new_c(:,2),'LineWidth',2.0)
hold;

%% to average the contour (line 1)
l=length(new_c(:,1));
x1=0;
y1=0;
for i=1:50
x1=x1+new_c(i,1);
y1=y1+new_c(i,2);
end
x1=x1/50;
y1=y1/50;
x2=0;y2=0;
for i=51:100
x2=x2+new_c(i,1);
y2=y2+new_c(i,2);
end
x2=x2/50;
y2=y2/50;
x3=0;y3=0;
for i=101:150
x3=x3+new_c(i,1);
y3=y3+new_c(i,2);
end
x3=x3/50;
y3=y3/50;

%% to average the contour (line 2)
x11=0;y11=0;
for i=(l-49):l
x11=x11+new_c(i,1);
y11=y11+new_c(i,2);
end
x11=x11/50;
y11=y11/50;

x22=0;y22=0;
```

```
for i=(l-100):(l-51)
x22=x22+new_c(i,1);
y22=y22+new_c(i,2);
end
x22=x22/50;
y22=y22/50;

x33=0;y33=0;
for i=(l-150):(l-101)
x33=x33+new_c(i,1);
y33=y33+new_c(i,2);
end
x33=x33/50;
y33=y33/50;

%% liner regression model
mdl1 = fitlm([x1 x2 x3],[y1 y2 y3]); % constant, slope
mdl2 = fitlm([x11 x22 x33],[y11 y22 y33]);
coeff1=mdl1.Coefficients.Estimate; %coefficients
coeff2=mdl2.Coefficients.Estimate; %coefficients

%% finding the intercepts (x0,y0)
m1=coeff1(2);
m2=coeff2(2);
c1=coeff1(1);
c2=coeff2(1);
x0=(c2-c1)/(m1-m2);
y0=m1*x0+c1;
plot(x0,y0,'r*','LineWidth',2.0);
new_x=new_c(:,1);
new_y=new_c(:,2);

%% find shortest distance
d=zeros(1,length(new_x));
g_best=100000;
for i=1:length(new_x)
p = [new_c(i,:);x0,y0];
d(i) = pdist(p,'euclidean');
if d(i)<g_best
    g_best=d(i);
    j=i;
end
end
plot(new_c(j,1),new_c(j,2),'b*','LineWidth',2.0);
xlim([50 400])
ylim([50 400])

%% plot points (optional)
plot([x1 x2 x3],[y1 y2 y3],'ko','LineWidth',2.0)
plot([x11 x22 x33],[y11 y22 y33],'ko','LineWidth',2.0)

%% orthogonal polish depth
pts=[x0,y0;new_c(j,1),new_c(j,2)];
dr = pdist(pts,'euclidean');  % radial overcut
pd=dr*sind(45);

%% acute polish depth
```

```
pts=[x0,y0;new_c(j,1),new_c(j,2)];
dr = pdist(pts,'euclidean');  % radial overcut
pd=dr*sind(15);

%% obtuse polish depth
pts=[x0,y0;new_c(j,1),new_c(j,2)];
dr = pdist(pts,'euclidean');  % radial overcut
pd=dr*sind(60);
```

Acknowledgement

The authors would like to acknowledge the central instrumentation facility, Indian Institute of Technology Palakkad for providing the test facilities.

Declarations

a. ***Funding:*** This research did not receive any specific grant from funding agencies in the public, commercial, or not-for-profit sectors.
b. ***Conflicts of interest/Competing interests:*** The authors declare that they have no known competing financial interests or personal relationships that could have appeared to influence the work reported in this paper
c. ***Availability of data and material:*** All data is available in the manuscript
d. ***Code availability:*** Not applicable
e. ***Ethics approval:*** Not applicable
f. ***Consent to participate:*** Not applicable
g. ***Consent for publication:*** Not applicable

References

1. Mahesh M, Wong YS, Fuh JYH, Loh HT (2004) Benchmarking for comparative evaluation of RP systems and processes. Rapid Prototyp J 10:123–135. https://doi.org/10.1108/13552540410526999

2. Moylan S, Slotwinski J, Cooke A, et al (2012) Proposal for a standardized test artifact for additive. Solid Freeform Fabrication Symposium 902–920

3. J.-P. Kruth, B. Vandenbroucke, J. Van Vaerenbergh PM (2005) BENCHMARKING OF DIFFERENT SLS/SLM PROCESSES AS RAPID MANUFACTURING TECHNIQUES. Int Conf Polymers & Moulds Innovations (PMI) 1–7. https://doi.org/10.3850/2424-8967_V02-N778

4. Vandenbroucke B, Kruth J-P (2007) Selective Laser Melting of Biocompatible Metals for Rapid. Rapid Prototyp J 13:148–159

5. Luo X, Li J, Lucas M (2017) Galvanometer scanning technology for laser additive manufacturing. Laser 3D Manufacturing IV 10095:1009512. https://doi.org/10.1117/12.2252973

6. Schwanekamp T, Bräuer M, Reuber M (2017) Geometrical and topological potentialities and restrictions in selective laser sintering of customized carbide precision tools. Proceedings of the Lasers in Manufacturing Conference

7. Han J, Wu M, Ge Y, Wu J (2018) Optimizing the structure accuracy by changing the scanning strategy using selective laser melting. Int J Adv Manuf Technol 95:4439–4447. https://doi.org/10.1007/s00170-017-1503-7

8. Braian M, Jönsson D, Kevci M, Wennerberg A (2018) Geometrical accuracy of metallic objects produced with additive or subtractive manufacturing: A comparative in vitro study. Dental Materials 34:978–993. https://doi.org/10.1016/j.dental.2018.03.009

9. Matache G, Vladut M, Paraschiv A, Condruz RM (2020) Edge and corner effects in selective laser melting of in 625 alloy. Manuf Rev (Les Ulis) 7:. https://doi.org/10.1051/mfreview/2020008

10. Zhihao F, Libin L, Longfei C, Yingchun G (2018) Laser Polishing of Additive Manufactured Superalloy. Procedia CIRP 71:150–154. https://doi.org/10.1016/j.procir.2018.05.088

11. Yung KC, Xiao TY, Choy HS, et al (2018) Laser polishing of additive manufactured CoCr alloy components with complex surface geometry. J Mater Process Technol 262:53–64. https://doi.org/10.1016/j.jmatprotec.2018.06.019

12. Worts N, Jones J, Squier J (2019) Surface structure modification of additively manufactured titanium components via femtosecond laser micromachining. Opt Commun 430:352–357. https://doi.org/10.1016/j.optcom.2018.08.055

13. Scherillo F (2019) Chemical surface finishing of AlSi10Mg components made by additive manufacturing. Manuf Lett 19:5–9. https://doi.org/10.1016/j.mfglet.2018.12.002

14. Jain S, Corliss M, Tai B, Hung WN (2019) Electrochemical polishing of selective laser melted Inconel 718. Procedia Manuf 34:239–246. https://doi.org/10.1016/j.promfg.2019.06.145

15. Peng C, Fu Y, Wei H, et al (2018) Study on Improvement of Surface Roughness and Induced Residual Stress for Additively Manufactured Metal Parts by Abrasive Flow Machining. Procedia CIRP 71:386–389. https://doi.org/10.1016/j.procir.2018.05.046

16. Tan KL, Yeo SH (2017) Surface modification of additive manufactured components by ultrasonic cavitation abrasive finishing. Wear 378–379:90–95. https://doi.org/10.1016/j.wear.2017.02.030

17. Zhang J, Chaudhari A, Wang H (2019) Surface quality and material removal in magnetic abrasive finishing of selective laser melted 316L stainless steel. J Manuf Process 45:710–719. https://doi.org/10.1016/J.JMAPRO.2019.07.044

18. Bagehorn S, Wehr J, Maier HJ (2017) Application of mechanical surface finishing processes for roughness reduction and fatigue improvement of additively manufactured Ti-6Al-4V parts. Int J Fatigue 102:135–142. https://doi.org/10.1016/j.ijfatigue.2017.05.008

19. Kaynak Y, Tascioglu E (2020) Post-processing effects on the surface characteristics of Inconel 718 alloy fabricated by selective laser melting additive manufacturing. Progress in Additive Manufacturing 5:221–234. https://doi.org/10.1007/s40964-019-00099-1

20. Boban J, Ahmed A (2021) Improving the surface integrity and mechanical properties of additive manufactured stainless steel components by wire electrical discharge polishing. J Mater Process Technol 291:117013. https://doi.org/10.1016/j.jmatprotec.2020.117013

21. Boban J, Ahmed A, Rahman MA, Rahman M (2020) Wire electrical discharge polishing of additive manufactured metallic components. Procedia CIRP 87:321–326. https://doi.org/10.1016/j.procir.2020.02.023

22. Zhang B, Jaiswal P, Rai R, et al (2019) Convolutional neural network-based inspection of metal additive manufacturing parts. Rapid Prototyp J 25:530–540. https://doi.org/10.1108/RPJ-04-2018-0096

23. Snow Z, Diehl B, Reutzel EW, Nassar A (2021) Toward in-situ flaw detection in laser powder bed fusion additive manufacturing through layerwise imagery and machine learning. J Manuf Syst 59:12–26. https://doi.org/10.1016/j.jmsy.2021.01.008

24. Grasso M, Demir AG, Previtali B, Colosimo BM (2018) In situ monitoring of selective laser melting of zinc powder via infrared imaging of the process plume. Robot Comput Integr Manuf 49:229–239. https://doi.org/10.1016/j.rcim.2017.07.001

25. Caggiano A, Zhang J, Alfieri V, et al (2019) Machine learning-based image processing for on-line defect recognition in additive manufacturing. CIRP Annals 68:451–454. https://doi.org/10.1016/j.cirp.2019.03.021

26. Akhil V, Raghav G, Arunachalam N, Srinivas DS (2020) Image Data-Based Surface Texture Characterization and Prediction Using Machine Learning Approaches for Additive Manufacturing. J Comput Inf Sci Eng 20:1–16. https://doi.org/10.1115/1.4045719

27. Kleszczynski S, zur Jacobsmühlen J, Sehrt JT, Witt G (2012) Error detection in laser beam melting systems by high resolution imaging. 23rd Annual International Solid Freeform Fabrication Symposium - An Additive Manufacturing Conference, SFF 2012 975–987

28. Abdelrahman M, Reutzel EW, Nassar AR, Starr TL (2017) Flaw detection in powder bed fusion using optical imaging. Addit Manuf 15:1–11. https://doi.org/10.1016/j.addma.2017.02.001

29. Caggiano A, Teti R, Alfieri V, Caiazzo F (2021) Automated laser polishing for surface finish enhancement of additive manufactured components for the automotive industry. Production Engineering 15:109–117. https://doi.org/10.1007/s11740-020-01007-1

30. Abhilash PM, Chakradhar D (2021) Failure detection and control for wire EDM process using multiple sensors. CIRP J Manuf Sci Technol 33:315–326. https://doi.org/10.1016/j.cirpj.2021.04.009

31. Abhilash PM, Chakradhar D (2020) ANFIS modelling of mean gap voltage variation to predict wire breakages during wire EDM of Inconel 718. CIRP J Manuf Sci Technol 31:153–164. https://doi.org/10.1016/j.cirpj.2020.10.007

32. Abhilash PM, Chakradhar D (2021) Wire EDM failure prediction and process control based on sensor fusion and pulse train analysis. Int J Adv Manuf Technol https://doi.org/10.1007/s00170-021-07974-8

33. Boban J, Ahmed A, Rahman MA, Rahman M (2020) Wire electrical discharge polishing of additive manufactured metallic components. Procedia CIRP 87:321–326. https://doi.org/10.1016/J.PROCIR.2020.02.023

34. Abhilash PM, Chakradhar D (2022) Performance monitoring and failure prediction system for wire electric discharge machining process through multiple sensor signals. Machining Science and Technology 26:245–275. https://doi.org/10.1080/10910344.2022.2044856

35. Abhilash PM, Chakradhar D (2022) Machine-vision-based electrode wear analysis for closed loop wire EDM process control. Adv Manuf 10:131–142. https://doi.org/10.1007/s40436-021-00373-y

36. Sanchez JA, Rodil JL, Herrero A, et al (2007) On the influence of cutting speed limitation on the accuracy of wire-EDM corner-cutting. J Mater Process Technol 182:574–579. https://doi.org/10.1016/j.jmatprotec.2006.09.030

37. Klocke F, Welling D, Klink A, Perez R (2014) Quality assessment through in-process monitoring of wire-EDM for fir tree slot production. New production technologies in aerospace industry - 5th machining innovations conference (MIC 2014)-Procedia CIRP 24:97–102. https://doi.org/10.1016/j.procir.2014.07.136

38. Fereiduni E, Ghasemi A, Elbestawi M (2020) Selective laser melting of aluminum and titanium matrix composites: Recent progress and potential applications in the aerospace industry. Aerospace 7:1–38. https://doi.org/10.3390/AEROSPACE7060077

39. Boban J, Ahmed A (2021) Improving the surface integrity and mechanical properties of additive manufactured stainless steel components by wire electrical discharge polishing. J Mater Process Technol 291:117013. https://doi.org/10.1016/j.jmatprotec.2020.117013

40. Boban J, Ahmed A (2022) Electric discharge assisted post-processing performance of high strength-to-weight ratio alloys fabricated using metal additive manufacturing. CIRP J Manuf Sci Technol 39:159–174. https://doi.org/10.1016/j.cirpj.2022.08.002